Version of Record: https://www.sciencedirect.com/science/article/pii/S0266352X24001186
Manuscript_e5a38012e387f882a58fda78c1fe59f6

Inverse Characterization of Shrinkage and Fracture of Bentonite Buffer Material for Geological Repositories of Nuclear Waste Using an Integrated DIC-FEM Approach

Mohammad Rahmani[a], Abdullah Azzam[a], Julia Grasley[a], Yong-Rak Kim[a,*], Jongwan Eun[b], Seunghee Kim[b]

[a] Zachry Department of Civil and Environmental Engineering, Texas A&M University, TX, USA
[b] Department of Civil and Environmental Engineering, University of Nebraska-Lincoln, NE, USA
*Corresponding author. Email address: yong-rak.kim@tamu.edu

ABSTRACT

This study presents an inverse method integrating the digital image correlation (DIC) and finite element modeling (FEM) to characterize the shrinkage and fracture of desiccating bentonite clay, considered a buffer material in engineered barrier systems for nuclear waste repositories. Rheology tests were conducted to measure elastic moduli of bentonite at various moisture contents, and a restrained ring test was designed and conducted to induce shrinkage followed by crack initiation and propagation due to the soil desiccation process. Due to the complex nature of characterizing multiphysical fracture parameters, especially for materials undergoing desiccation cracking, an inverse method was employed. The full-field displacement of the desiccating bentonite, captured by DIC, was used to calculate shrinkage-induced stresses. A boundary value problem representing the test conditions was modeled through the finite element method incorporated with cohesive zone elements to simulate the shrinkage-induced cracking. The moisture-dependent shrinkage and fracture parameters of bentonite were inversely characterized through an optimization process, where material parameters in FEM were iteratively calibrated to ensure that the simulated full-field displacements before the onset of cracking and subsequent crack dimensions agreed well with the experiment. The novel experimental-computational method can identify evolving material characteristics subjected to complex hygro-mechanical conditions with fracture damage.

Keywords: Inverse optimization, Engineered barrier material, Bentonite, Desiccation cracking, Finite element model, Cohesive zone fracture, Digital image correlation.

© 2024 published by Elsevier. This manuscript is made available under the Elsevier user license
https://www.elsevier.com/open-access/userlicense/1.0/

1. Introduction

In many engineering applications, such as designing engineered barrier systems (EBS) at geological repositories, the designated material [bentonite clay] is exposed to a relatively high temperature, leading to water evaporation and subsequent shrinkage of the soil adjacent to the nuclear spent-fuel canisters (Alonso et al., 2005; H. Chen, Lv, Chen, & Li, 2019; Graupner et al., 2018; Rutqvist, 2020; Rutqvist, Börgesson, Chijimatsu, Nguyen, et al., 2001). Since the buffer material in geological repositories is surrounded by hard natural rocks from one side and the canisters from another, the induced shrinkage process becomes mechanically restrained, leading to the development of tensile stress within the clayey soil (Nahlawi, Chakrabarti, & Kodikara, 2004). Desiccation cracking happens when the stresses exceed the material limit (Hassanikhah, Miller, & Cerato, 2021). Cracking can increase the permeability of the buffer medium and elevate the risk of generating potential pathways for the water to infiltrate into the EBS and degrade the canisters.

With the progression of desiccation in soil, its mechanical and hydraulic properties can significantly alter (Aruna L Amarasiri & Kodikara, 2013; Byun, Lee, Cho, & Yoon, 2013; Kodikara & Choi, 2006; Ross A Stirling, Hughes, Davie, & Glendinning, 2015). Since EBSs are designed to provide long-term confinement and isolation of nuclear spent fuels [more than a hundred thousand years] (Lutzenkirchen, 2006), it is imperative to understand the evolution of the buffer material properties and its geomechanical response throughout the lifetime of a geological repository (Rutqvist, Ijiri, & Yamamoto, 2011; Rutqvist, Zheng, Chen, Liu, & Birkholzer, 2014).

The key parameters which mainly characterize the initiation and propagation of tensile cracks, as a major and critical issue associated with buffer materials, are tensile strength and fracture energy (Le, Liu, Tang, Zhang, & Shi, 2022). In the context of the cohesive zone model, tensile strength is the maximum normal traction on cohesive surfaces beyond which the material behavior irreversibly transfers from elastic to damage-associated, and fracture energy is the energy required to completely separate the cohesive surfaces. Characterizing these fracture parameters for materials like soils is an inherently complex task, made even more challenging when they are subjected to multiphysics processes such as desiccation cracking. To characterize crack initiation mechanism, (Nahlawi et al., 2004; Zeng, Yu, Gao, Liu, & Liu, 2022) adopted a simplifying approach, employing a direct tensile test on clayey soils at varying water contents.

This technique facilitated the capture of a specific range of suction that the soil typically experiences during the desiccation process. They observed that the tensile strength increased nonlinearly with the reduction of water content. However, direct measurement of evolving fracture parameters from desiccating bentonite is very limited to the author's knowledge as it often proves elusive due to the intricate nature of this multiphysics process. Therefore, an inverse approach becomes a more favorable alternative, providing a viable pathway to estimate these parameters with justifiable accuracy.

In the inverse method, the experimental measurement and numerical simulations or analytical solution can be coupled forming, a loop of calibration and validation. Instead of merely relying on the global response of material from conventional direct or indirect tensile tests, local response (such as field displacement) with high-fidelity information on heterogeneity, anisotropy, and fracture can be used to characterize the tensile behavior of the soil inversely. The field displacement measured during the testing can be captured by a digital image correlation (DIC) system (McCormick & Lord, 2010; Yoneyama, 2016). DIC technically captures pixel movement from successive images and correlates them to equivalent deformation gradient (Nsengiyumva & Kim, 2022). Many researchers integrated DIC with the finite element modeling (FEM) to inversely identify the elastic or inelastic material model parameters (Gerbig, Bower, Savic, & Hector Jr, 2016; Hartmann, Gilbert, Marghzar, Leistner, & Dileep, 2021; Junior, Borges, Araújo, & Pituba, 2021; Mathieu, Leclerc, Hild, & Roux, 2015; Nsengiyumva & Kim, 2022). The identification procedure is usually based on an optimization problem in which the numerical or analytical solution of a particular boundary value problem is compared to its corresponding experimental result (Ogierman, 2018).

Numerical models often provide the inverse optimization process with the necessary input to be compared to the testing. In the context of material fracture simulation, different numerical techniques can be utilized, such as cohesive zone model (CZM) (Pouya, Vo, Hemmati, & Tang, 2019; Vo, Pouya, Hemmati, & Tang, 2017), discrete element method (DEM) (Le et al., 2022; Z.-Y. Lin et al., 2021; Peron, Delenne, Laloui, & El Youssoufi, 2009; Sima, Jiang, & Zhou, 2014), finite discrete element method (FDEM) (Cai, Gao, Ai, Wang, & Feng, 2023; C. Yan, Wang, Ke, & Wang, 2021; C. Yan, Zheng, Ke, & Wang, 2021), and Peridynamics (H. Yan, Jivkov, & Sedighi, 2023; Zhao et al., 2021). The CZM is a fracture-mechanics approach that is extensively used to model cracking in various materials. The fracture formation in a

general CZM is regarded as a gradual phenomenon in which the separation of surfaces occurs in a potential damage zone ahead of a crack tip. CZM can simulate multiple cracks simultaneously in their various stages (initiation, propagation, and coalescence) when integrated with FEM (Y.-R. Kim, 2011; Y.-R. Kim, Aragao, Allen, & Little, 2010; Y. R. Kim et al., 2021; Pouya et al., 2019; Rahmani & Kim, 2020; Rahmani, Kim, Park Yong, & Jung Jong, 2020; Rahmani, Nsengiyumva, Kim, & Hu, 2020).

This study aims to characterize the shrinkage and fracture of desiccating bentonite clay, often considered a buffer material in engineered barrier systems (EBS) for nuclear waste repositories. Due to the complex nature of the multiphysics phenomenon, this study attempts to develop a novel integrated DIC-FEM approach enhanced by a crack detection algorithm to efficiently characterize the shrinkage and cohesive zone fracture parameters of desiccating bentonite clay. The following sections describe the research methodology, laboratory tests, finite element modeling details, and inverse identification process and results.

2. Research Methodology

This study hypothesizes that the full-field displacement and strain measurements at the surface of the desiccating bentonite clay sample can be used in an inverse analysis to determine the shrinkage and fracture properties of the clay. An important material parameter, hygroscopic expansion coefficient, quantifies the degree of shrinkage per unit decrease in water content and it directly influences the displacements and strains that arise in the material as it desiccates. In the context of cohesive fracture, the displacement and strain fields are directly related to the material's fracture properties through the traction-separation constitutive relation, which defines how the material responds when cohesive boundaries start to separate. Laboratory tests were designed and conducted for bentonite samples to analyze their restrained shrinkage behavior. The ring test represents a condition where a mechanical constraint causes tensile stress development within the material. A DIC system was set to record and analyze the full-field displacements and their derivatives (strains).

The fundamental principle of the DIC-FEM inverse approach is minimizing the discrepancy between the DIC-measured displacement field and the calculated displacement field from a FE modeling of the same geometry and boundary conditions as testing. The nonlinear optimization process, which utilizes the Nelder-Mead algorithm (Lagarias, Reeds, Wright, &

Wright, 1998; Nelder & Mead, 1965; Singer & Nelder, 2009) in this paper, iteratively calibrated the FE model parameters until there is no significant change in the objective function value (i.e., difference between DIC- and FEM-driven displacement fields). The radial and circumferential hygroscopic expansion coefficient, moisture-dependent tensile strength, and moisture-dependent fracture energy were inversely identified using this method. The process of inverse identification of material parameters is illustrated in Figure 1.

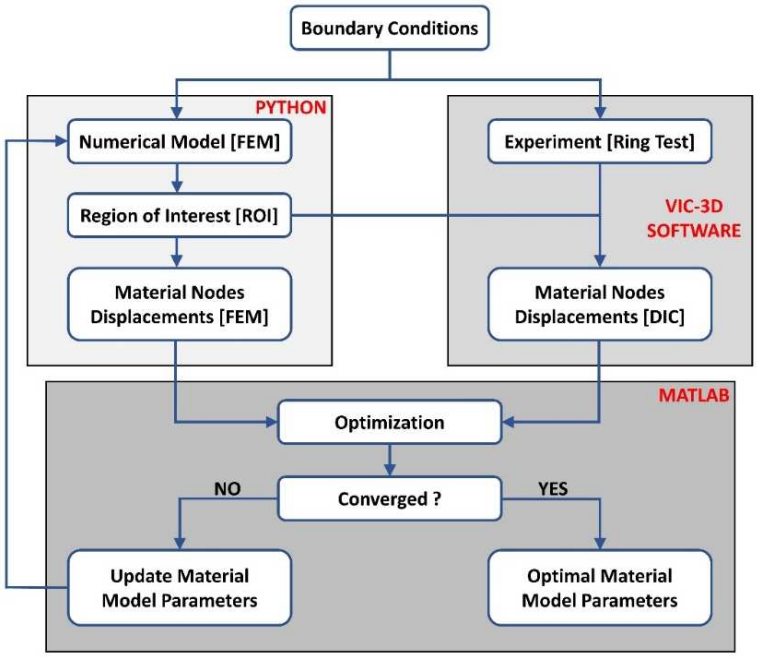

Figure 1. Process of inverse identification of material parameters.

3. Laboratory Experiment

3.1. Restrained ring test

Pure Wyoming bentonite (MX-80) was used in this study. The oven-dried fine-grinded bentonite clay (with a diameter of less than 75 µm) was used to fabricate samples. The physical properties of bentonite are represented in Table 1, and the details on mineral composition can be found in (Montes-H & Geraud, 2004; Savage, Arthur, & Luukkonen, 2012). Samples were prepared in a wet slurry condition (water content around the liquid limit) to ensure the uniformity of the mixture. An oedometer ring with 100 mm diameter and 10 mm thickness was used to mold each specimen followed by a consolidation step to ensure uniform moisture distribution and minimize the internal defects. To make the ring-shaped sample, a stainless-steel ring with a 30

144 mm outer diameter perforated the middle of the disc-shaped sample. It should be noted that
145 moisture evaporation was only allowed from the top surface of the specimen due to the small
146 thickness and lubrication coating with petroleum jelly on the side and bottom of the specimens.
147 Lubrication coating was also applied to the soil-ring interface to minimize the friction in that
148 area. Two DIC cameras were set up above the samples to record their surface displacements
149 during the shrinkage process. Figure 2 shows an image of the test setup. All testing was
150 conducted in the laboratory at a controlled condition of 22 ^{o}C and relative humidity of 40%.
151 Three replicates of each mixture were prepared and tested to obtain repeatable results. It should
152 be noted that the experiment and sample conditions are limited and differ from realistic
153 conditions at the geological repository of nuclear spent fuel. Although limited and somewhat
154 apart from the realistic repository condition of the materials, the testing was adopted in this study
155 as a baseline effort to first understand the desiccation process of bentonite clay including its
156 shrinkage and subsequent cracking by incorporating computational modeling. To do so, sample
157 condition in particular spatial consistency (i.e., homogeneity) was crucial, and higher moisture
158 content within the sample can lead to minimized internal defects and heterogeneities. Thus, the
159 experiment in this study was conducted under controlled conditions to provide a basis for the
160 systematic characterization of key parameters of multiphysical behavior (i.e., shrinkage and
161 moisture-dependent fracture due to the desiccation process).
162
163 Table 1. Physical Properties of Bentonite Used in This Study

Soil properties	Values
Specific gravity	2.69 (Ravi & Rao, 2013)
Bulk density	1.066 g/cm^3
Swell index	32 mL/2g (IV et al., 2018)
Liquid limit	400%
Plastic limit	95%
Shrinkage limit	12.2% (Tripathy, Tadza, & Thomas, 2014)
Plasticity index	305
Initial dry density	0.188 g/cm^3
Initial porosity	93%
Initial volumetric water content	501.1%

164
165

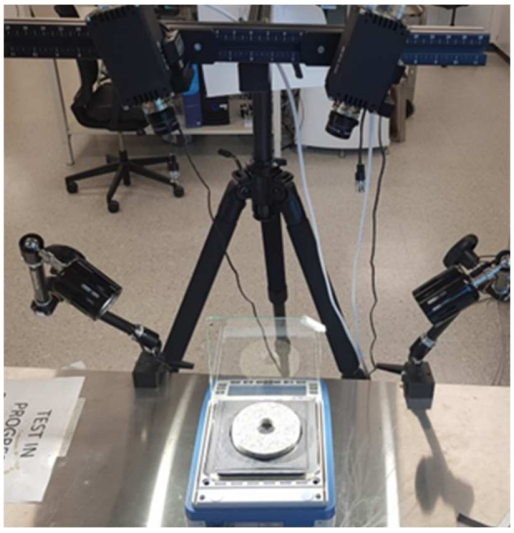

Figure 2. Restrained ring specimen with the DIC setup.

166

167 *3.2. Rheology test for moisture-dependent elastic modulus*

168 Considering the effect of water content on the elastic modulus is essential for reliable
169 predictions of the mechanical behavior of soils in numerical simulations. The bentonite used in
170 this study is presumed to feature nonlinear elastic behavior with the monotonic change of
171 stiffness with water content, which is acceptable because strain reversal is not prevalent due to
172 continuous drying (Aruna L. Amarasiri, Kodikara, & Costa, 2011). In many other studies, the
173 elastic modulus was defined as an exponential function of water content (Le et al., 2022; Z. Y.
174 Lin et al., 2022; Sima et al., 2014; Ross A. Stirling, Glendinning, & Davie, 2017).

175 To obtain the moisture-dependent elastic modulus of bentonite, rheology tests were
176 conducted for seven samples mixed with different gravimetric water contents (i.e., 500%, 400%,
177 300%, 200%, 100%, 50%, and 30%). Each case was tested with three replicates to ensure the
178 consistency of the results. For samples with higher water contents (equal or higher than 100% or
179 in slurry condition), parallel plates were used where a thin disc sample (1.6 mm thick) was
180 placed between two disc-shaped plates and subjected to a cyclic torsional strain range from
181 0.01% to 10% at 1 Hz frequency. For stiffer samples (less than 100% water content), a
182 cylindrical rod bentonite specimen (10.4 mm diameter and 31 mm height) was used and
183 subjected to a cyclic torsional strain range of 0.0001% to 1% at 1 Hz frequency. The
184 experimental result of moisture-dependent elastic modulus is shown in Figure 3. Different water
185 contents represent the stages of desaturation and cover a range of suctions that bentonite clay

experiences during the desiccation process. The volumetric water content and saturation level were calculated based on the experimental results, and the suction level was estimated according to (T. Chen, Du, & Yao, 2022). As shown in Figure 3, the elastic modulus of bentonite increased with a reduction in water content. A second-order exponential function was fitted to the moisture-dependent Young's moduli to cover the data set as follows.

$$E = a_1 e^{a_2 \cdot w} + a_3 e^{a_4 \cdot w} \quad (1)$$

where, w is gravimetric water content in percent, $a_1 = 880.244$, $a_2 = -0.0689$, $a_3 = 0.2547$, and $a_4 = -0.0014$.

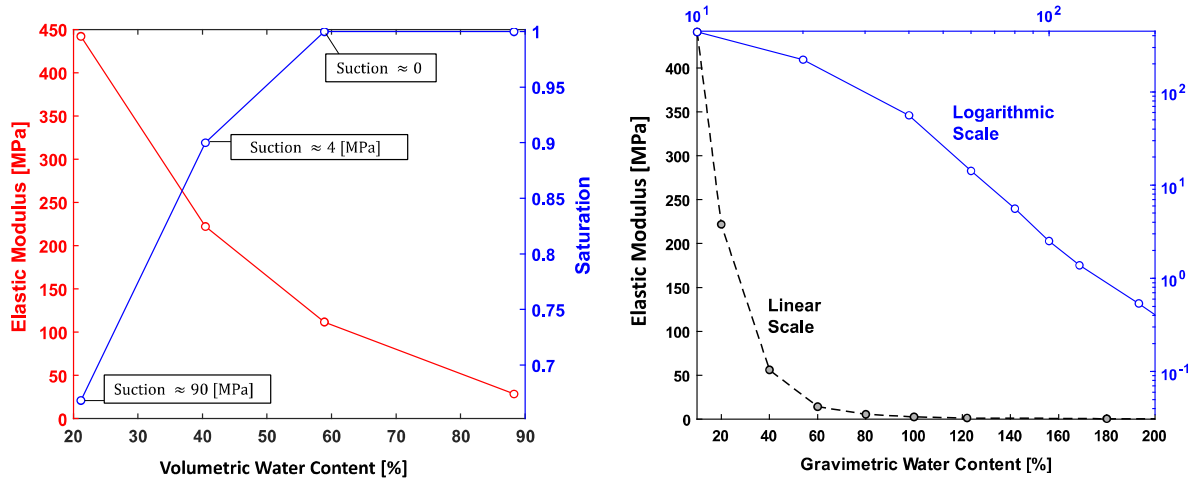

4. Numerical Modeling of Desiccation Cracking

4.1. Desiccation process

The moisture diffusion within the sample domain, J (kg m^{-2}s^{-1}), can be described by the Fick's law.

$$J = -D\nabla C \quad (2)$$

where D is moisture diffusivity (m^{2}s^{-1}) and C is moisture concentration (kg m^{-3}). Assuming no substance generation and spatial-invariance of D, the mass conservation law leads to moisture diffusion equation as follows.

$$\frac{\partial C}{\partial t} = D\nabla^2 C \quad (3)$$

202 The convective moisture flux boundary condition can be defined through Newton's law
203 as follows.

$$J_s = -h(\mathrm{C}_s - \mathrm{C}_{env}) \quad (4)$$

204 where, h is surface film coefficient ($\mathrm{m}^1\mathrm{s}^{-1}$), C_s is moisture concentration at exposed surface,
205 and C_{env} is ambient moisture concentration.

206 *4.2. Conservation of momentum and constitutive model*

207 The Cauchy's first law of motion can be written as

$$\rho \frac{\partial^2 u_i}{\partial t^2} = \rho b_i + \frac{\partial \sigma_{ij}}{\partial x_i} \quad (5)$$

208 Considering quasi-static condition ($\frac{\partial^2 u_i}{\partial t^2} = 0$) in the absence of body forces ($\rho b_i = 0$), the
209 equilibrium equation can be simplified to

$$\frac{\partial \sigma_{ij}}{\partial x_i} = 0 \quad (6)$$

210 where σ_{ij} is the stress tensor.

211 The total strain increment can be split into mechanical strain increments $d\varepsilon_{ij}^m$ and
212 hygroscopic strain increments $d\varepsilon_{ij}^h$ as shown in Equation (9).

$$d\varepsilon_{ij} = d\varepsilon_{ij}^m + d\varepsilon_{ij}^h \quad (7)$$

213 The incremental nonlinear constitutive relation considering tangential stiffness tensor
214 (which is coupled with moisture concentration field) and hygro-mechanical strains in a fully-
215 saturated medium can be written in the following form. It should be noted that the
216 comprehensive field equations and FEM formulations for partially saturated soil media can be
217 found in (Rutqvist, Börgesson, Chijimatsu, Kobayashi, et al., 2001).

$$d\sigma_{ij} = D_{ijkl}\, d\varepsilon_{kl}^m = D_{ijkl}\left(d\varepsilon_{kl} - d\varepsilon_{kl}^h\right) = D_{ijkl}(d\varepsilon_{kl} - \beta\, dw\, \delta_{kl}) \quad (8)$$

218 where β is the hygroscopic expansion coefficient and the relation between incremental change in
219 gravimetric water content and moisture concentration is $dw = dC/\rho_d$.

220 The investigated bentonite's response to the water content decrement was observed to be
221 anisotropic during the experiments. Shrinkage in radial and circumferential directions occurred at
222 different rates. It was also observed that the shrinkage strain increments in both directions were
223 linearly related to the change in water content (Peron, Hueckel, Laloui, & Hu, 2009).
224

4.3. Boundary conditions and stress distribution

To model water evaporation from the top boundary of the samples, the convective moisture flux boundary condition was defined. The choice of applying this flux boundary condition to the top surface was based on the specific experimental setup of the samples, where the peripheral sides and bottom of the samples were lubricated and isolated to prevent moisture flux. The convective moisture flux from the experiment was measured, and the resulting value is $3.88*10^{-5}$ [kg/m^{2}s]. This convective boundary condition was defined through surface flux to model out-of-plane flux to be consistent with the 2D model. Figure 4 illustrates the definition of convective flux boundary condition. Figure 5(a) schematically shows the experimental implementation of the boundary condition, ensuring that the moisture flux occurs only from the top surface.

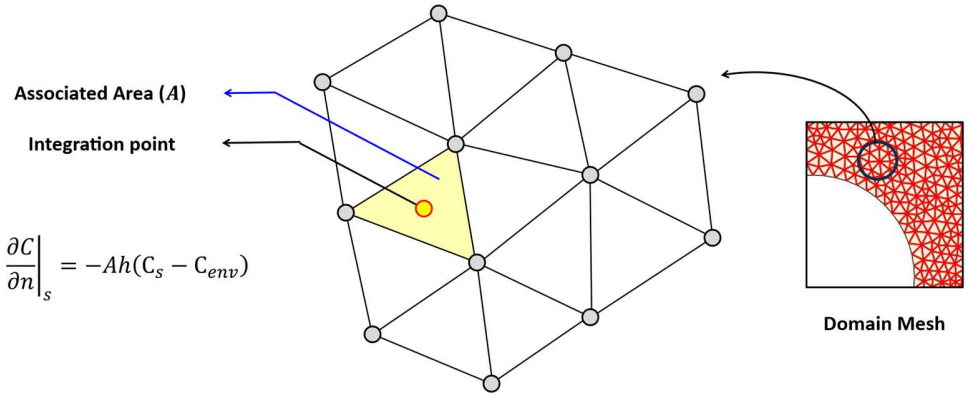

Figure 4. Illustration of the convective flux boundary condition.

The associated nodal area approximates the area associated with each integration point. This area term is needed because convective transport is proportional to the area through which the water content is transported. The average element area (i.e., $\sqrt{3}$) was used in the analysis.

In a free shrinkage test (e.g., shrinking disc), no stress is developed due to the absence of mechanical constraint. However, in the ring test, which represents a restrained shrinkage process, a metal ring much stiffer than bentonite clay that is placed in the middle of the sample, limits the radial deformation of the sample during shrinkage. While the normal displacement is set to zero at the ring-soil interface, circumferential displacements occur [accommodated by lubrication of the interface], which causes tensile stress to develop. If the induced tensile stress exceeds the

material limit, desiccation cracks will initiate. Figure 5(b) illustrates the stress distribution in a ring-shaped sample.

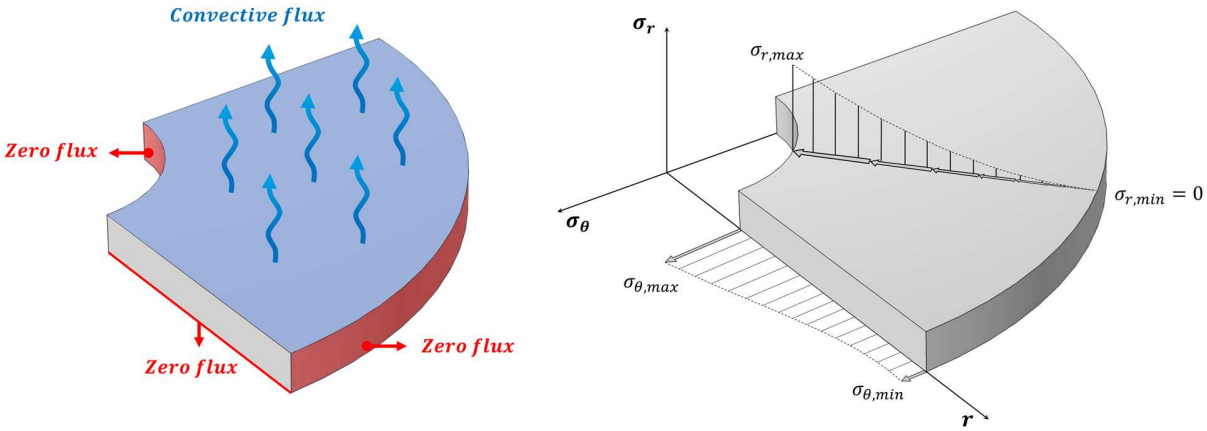

(a) (b)

Figure 5. (a) Moisture boundary condition; and (b) stress distribution in a restrained ring sample.

4.4. Cohesive zone model

Among various fracture mechanics-based approaches to model initiation and propagation of cracks, cohesive zone modeling has been used due to its straightforward implementation in the FEM and the capability to model multiple cracks simultaneously. This study used a bilinear cohesive zone model to effectively simulate the desiccation cracking of bentonite clay. According to the model concept, the fracture is resisted by cohesive tractions that first reach a maximum value T_{max}, where the cohesive zone (or fracture process zone) starts to degrade, and the material behavior is no longer recoverable elastic. The cohesive traction subsequently reduces to 0 (zero), where the surfaces are entirely separated. Figure 6 illustrates the process of cracking with the bilinear cohesive zone model.

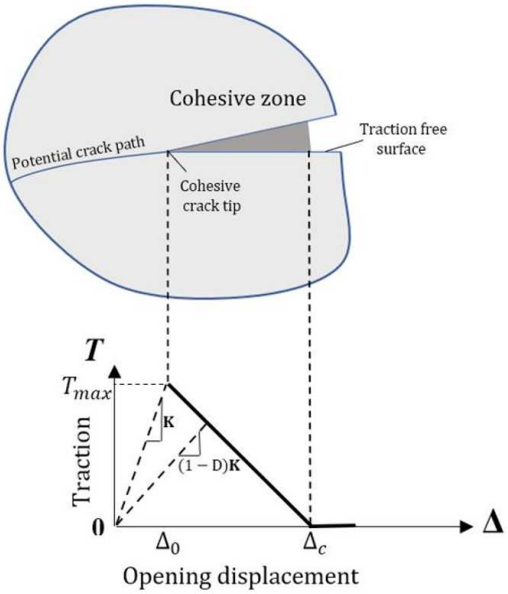

Figure 6. Schematic illustration of the bilinear cohesive zone model.

The bilinear cohesive zone constitutive behavior is expressed in the following equation, where the cohesive zone traction is related to the crack opening displacement controlling initiation and evolution of damage.

$$T_n = (1 - D)K_p\Delta_n$$
$$D = \frac{\Delta_c(\Delta_{max} - \Delta_0)}{\Delta_{max}(\Delta_c - \Delta_0)} \quad (9)$$

where T_n is the normal traction vector acting on the cohesive zone boundary, D is the scalar damage variable, K_p is the penalty stiffness, Δ_n is cohesive zone normal separation, Δ_{max} is the maximum separation of the cohesive boundaries in the loading history, and Δ_c is the critical separation displacement at failure.

The cohesive zone fracture energy, Γ_c, which is the energy required to separate the cohesive faces fully, can be calculated by computing the area under the traction-separation bilinear curve with the maximum traction T_{max} (traction at crack initiation) and Δ_c (critical opening displacement) where the cohesive zone faces are irreversibly separated. Equation (10) is the cohesive zone fracture energy using the bilinear cohesive zone model.

$$\Gamma_c = \frac{1}{2}\, T_{max}\, \Delta_c \quad (10)$$

4.5. Finite element model

A two-dimensional plane stress FE model was generated, and domain geometry for the ring and mechanical boundary conditions were set similarly to the testing conditions. The inner and outer radii of the ring-shaped sample were set to 15 mm and 50 mm, respectively. To model the restrained shrinkage process, the radial displacement of the domain is set to zero at the soil-ring interface, while circumferential displacement is allowed. Figure 7(a) shows the FE model mesh structure and mechanical boundary conditions imposed on the restrained ring model. A mesh size of 2mm was chosen after a thorough mesh sensitivity analysis to ensure the convergence of solutions (see Figure 10). An in-house code was used to place the zero-thickness cohesive elements throughout the domain. This way enables random initiation and propagation of cracks within the domain. The cohesive zone elements are embedded between each pair of adjacent triangular elements. The analysis flowchart is depicted in Figure 7(b).

(a)

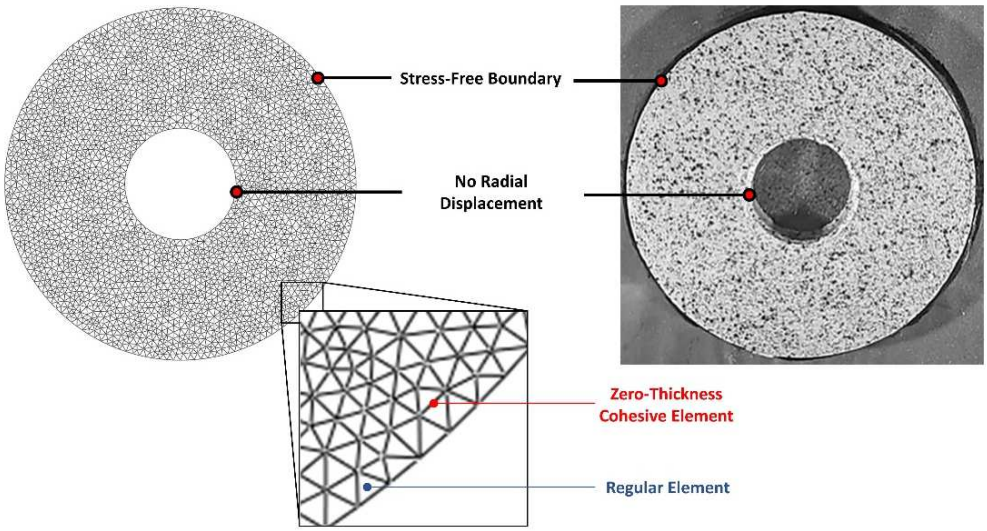

(b)

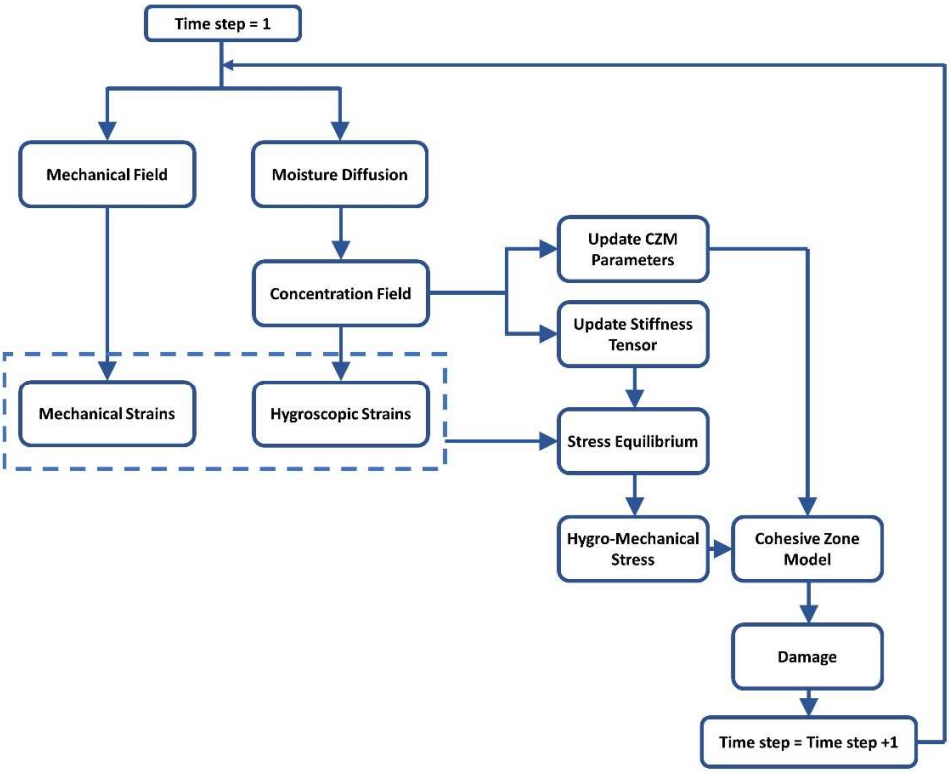

Figure 7. (a) FEM Mesh and boundary conditions, and (b) analysis flowchart.

5. Inverse Material Parameter Identification

The inverse method was utilized to characterize the hygroscopic expansion coefficients and the cohesive zone model parameters for bentonite clay, considering the latter parameters as functions of the water content. The inverse method was systemized based on penalizing the discrepancy between experimentally- and numerically-driven local displacement fields. An in-house Python code was used to iteratively calibrate the material model parameters, run the FE model (using Abaqus CAE) (Systèmes, 2014), obtain the numerical results, run the optimization algorithm, update the parameters, and redo this process until the stopping criterion was satisfied.

5.1. Optimization process

The inverse identification of material parameters was carried out in three sequentially coupled steps. In the first step, the optimal values for hygroscopic expansion coefficients in both radial and circumferential directions were back-calculated. The full-field displacements from DIC and FEM were used in the process. To validate the numerical results, strains at random locations within the ring domain were compared to the experiment. The second step focused on

the crack initiation and cohesive zone tensile strength (T_{max}) of bentonite which was considered a power function of gravimetric water content with two material parameters. There are many other studies in which the tensile strength of a desiccating soil was implemented in the numerical model as a power function (Aruna L. Amarasiri et al., 2011; Kodikara & Choi, 2006; Nahlawi et al., 2004). In the third step, crack propagation governed by the cohesive zone fracture energy was characterized. A power function for the fracture energy with two material parameters was hypothesized, and the resulting parameters were calibrated iteratively, so the yielded crack pattern and crack opening displacement from FE modeling agree well with the experimental results for ring-shaped bentonite samples.

5.2. Objective function

An objective function incorporating experimental and numerical displacement fields was defined and used in the optimization process. The FEM and DIC-driven displacement field vectors were measured at the number of paired DIC-FEM nodes, N_n. For each node, the FEM displacement field vector is measured for the number of unknown parameters, N_p, which is two for each optimization step: radial and circumferential hygroscopic expansion coefficients in the first step, two material parameters for cohesive zone tensile strength in the second step, and two material parameters for the cohesive zone in the third step. Then, the square of the Euclidean norm of the difference between the FEM and DIC displacement field vectors, obtained for all the nodes, is summed. The measure of discrepancy is expressed in the following equation:

$$\Phi(\xi) = \sum_{j=1}^{N_p} \sum_{i=1}^{N_n} \left\| u_{DIC}^{(i,j)} - u_{FEM}^{(i,j)}(\xi) \right\|_2^2 \tag{11}$$

where $\Phi(\xi)$ is called the objective function; ξ is the set of unknown parameters (e.g., coefficients of shrinkage) used for each one of the FEM simulations; $u_{DIC}^{(i,j)}$ and $u_{FEM}^{(i,j)}(\xi)$ are the displacement field vectors at the node i for the j^{th} value of unknowns.

5.3. Optimization algorithm

The Nelder-Mead simplex-based solver was used due to its robustness and ease of implementing constraint functions. The details on the Nelder-Mead algorithm can be found in the related references (Lagarias et al., 1998; Singer & Nelder, 2009).

6. Results and Discussion

6.1. Moisture loss with time

The desiccation process and temporally-variant concentration field were modeled in FEM through convective mass flux. The nonlinear elastic model is one-way coupled with the moisture concentration field so that in each time step, the tangent stiffness matrix is calculated based on the moisture-dependent elastic modulus (described in section 3.2). The average convective mass flux across the top boundary (through evaporation) measured from the experiment was $3.88*10^{-5}$ [kg/m^{2}s], which is consistent with previous studies on similar material (Tamizdoust & Ghasemi-Fare, 2022). The moisture loss modeled in FEM was characterized by convective moisture transfer coefficient, h, and was calibrated with the experimental result of moisture concentration. The Poisson's ratio was 0.43 for the bentonite used in this study. The value of the Poisson's ratio was reasonably assumed to be constant as the material was close to fully-saturated level up to the onset of cracking (Aruna L Amarasiri & Kodikara, 2013; Aruna L. Amarasiri et al., 2011). The data used in FEM for moisture field analysis is presented in Table 2.

Table 2. Model Parameters for Moisture Diffusion Analysis

Parameter	Value
Initial gravimetric water content [%]	465
Diffusion coefficient $[\frac{m^2}{s}]$	2×10^{-9}
Convective moisture transfer coefficient $[\frac{m}{s}]$	0.0147

The temporal evolution of moisture content in the ring-shaped sample and its subsequent desiccation-induced shrinkage, which is further discussed in the following subsection, is shown in Figure 8. As can be seen, the water content distribution within the domain is uniform due to a simplified convective moisture flux boundary condition imposed at the surface of the sample to model the water evaporation. The experimental and numerical results for water content were compared, and it can be inferred that the numerical model could effectively simulate the desiccation process.

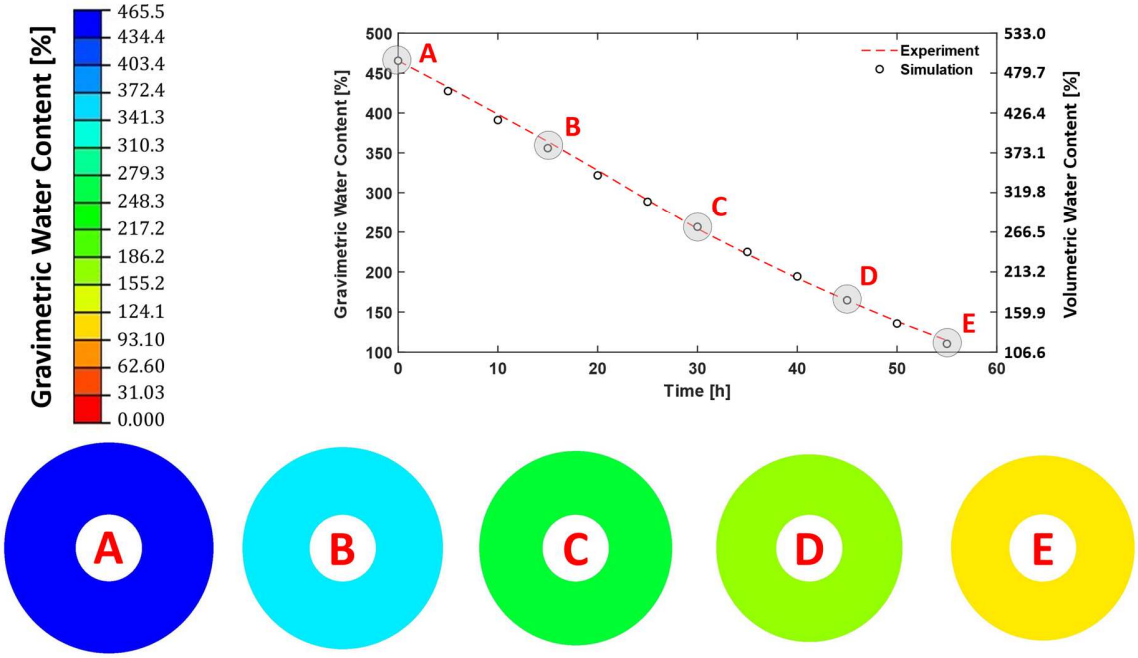

Figure 8. Numerical and experimental results of water content.

355

356 *6.2. Shrinkage behavior*

357 The first step of the optimization process focused on the shrinkage behavior of the
358 bentonite up to the onset of cracking. The distinction between these two processes (i.e.,
359 shrinkage and cracking) allows us to capture the pure shrinkage behavior of the clay and the
360 later-stage cracking induced by shrinkage. The FEM and DIC nodes in this step matched well at
361 the same coordinates. Orthotropic shrinkage behavior was observed for the bentonite clay
362 samples during their desiccation. As shown in Figure 9, the shrinkage in the radial direction was
363 more significant than in the circumferential direction. Therefore, two material parameters, radial
364 and circumferential (hoop) hygroscopic expansion coefficients, were iteratively calibrated in the
365 optimization process until the FEM displacement field matched its counterpart from DIC.

(a)

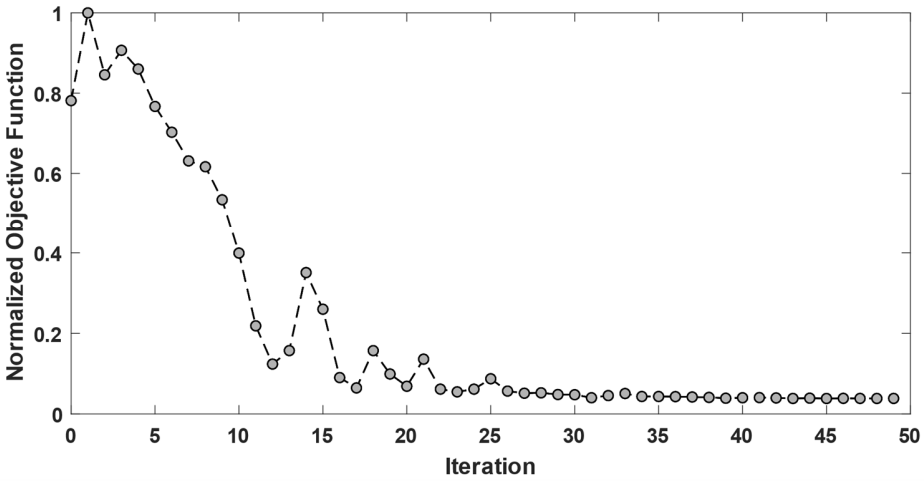

(b)

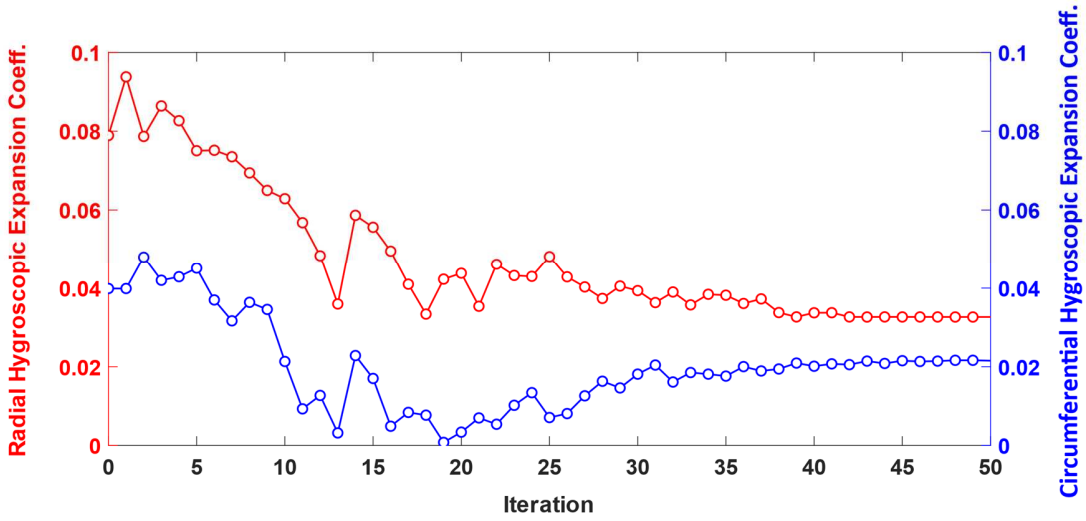

Figure 9. Inverse determination of hygroscopic expansion coefficients: (a) stabilized objective function value over iteration, and (b) optimal model parameters saturated from the iteration.

As can be seen in Figure 9(a), the normalized objective function value, which represents the discrepancy between the numerical and experimental results (displacement fields), was minimized through updating the hygroscopic expansion coefficients, iteratively. The optimal values were selected when the difference in objective function values of consecutive iterations was smaller than a pre-determined value (10^{-4}). The obtained values for hygroscopic expansion coefficients are reasonable compared to other studies on similar materials (Guo, Han, & Yu, 2018; Sima et al., 2014; C. Yan, Wang, et al., 2021).

The resulting hygroscopic expansion coefficients were used in this study for model simulations. This simplification with constant hygroscopic expansion coefficients is based on the fact that the shrinkage-induced deformation in this study occurred at a degree of saturation very close to 100%, where the decrease in the sample volume during desiccation is likely identical to the reduction in the volume of water (Lu & Dong, 2017; Peron, Delenne, et al., 2009). They reported a minimal variation in hygroscopic expansion coefficients under fully saturated conditions and used a constant value for shrinkage analysis. In other studies (Chertkov, 2003; Hobbs, Jones, Kirkham, Gunn, & Entwisle, 2019) on clay shrinkage, the nonlinearity in the relation of water content decrement and volumetric shrinkage of clays occurs at the water content level below the shrinkage limit. Considering that the volumetric water content of the samples in this study did not reach the shrinkage limit (12.2%), constant hygroscopic expansion coefficients were assumed, which provides great efficiency for the modeling and characterization process. However, it is not certain if the constant hygroscopic expansion coefficients are maintained after significant desiccation cracks are formed, as the post-crack deformation behavior is likely nonlinear, which requires further studies and is not fully addressed in this study.

For the FE modeling, a thorough mesh sensitivity analysis was performed to ascertain that the simulation results are independent of a specific mesh structure, and the selected mesh provides convergent solutions. Figure 10 shows the results of mesh convergence study demonstrating the radial displacements of the domain's outer boundary and the radial strains at the ring-soil interface. Based on the results, the mesh size of 2 mm was chosen.

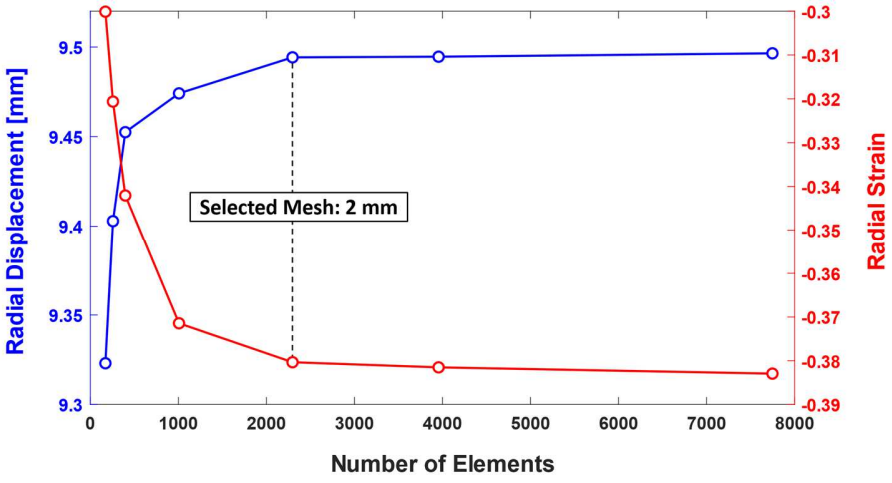

Figure 10. Results of mesh sensitivity analysis.

The horizontal and vertical displacements at four random locations within the ring-shaped domain were compared to the experiment result to demonstrate the validity of the inversely identified hygroscopic expansion coefficients. Figure 11 shows that the FEM and DIC results at the four randomly-selected locations match very well. This validation process confirms that the material parameters found from the global optimization process considering the entire displacement field are valid and reasonable, which further assures that the identified hygroscopic expansion coefficients can be used for further modeling of desiccation cracking.

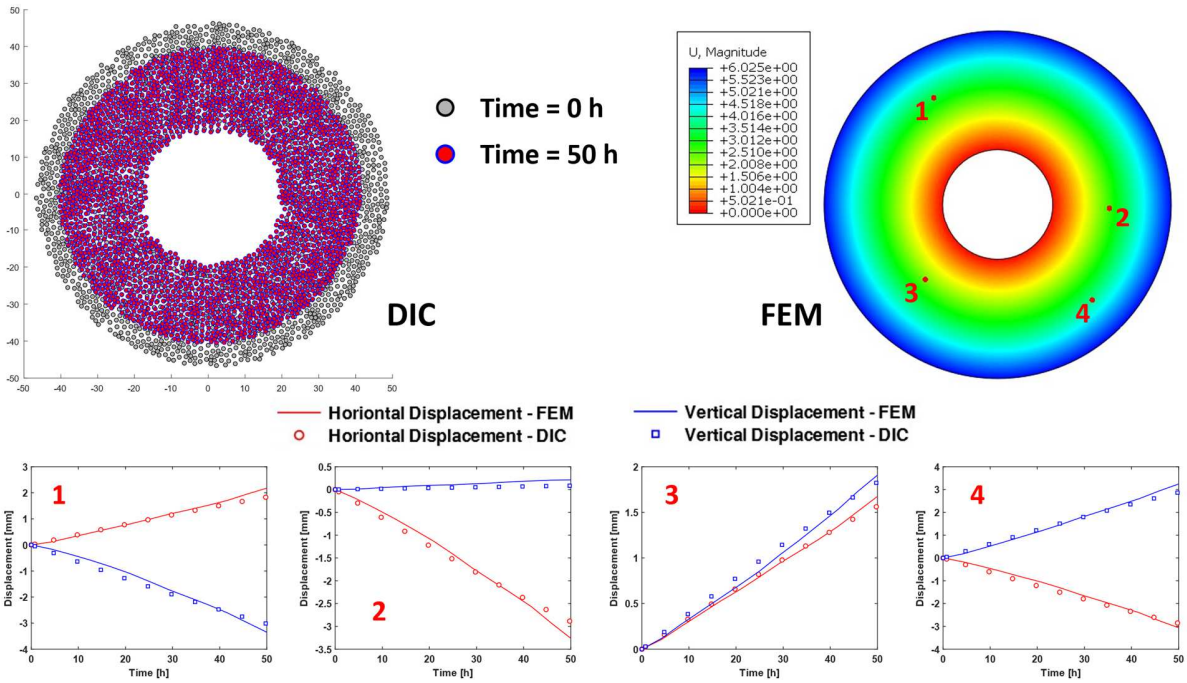

Figure 11. Results from the DIC-FEM inverse method for hygroscopic expansion coefficients: comparison of displacements at the four randomly-selected locations.

6.3. Desiccation crack modeling

As mentioned earlier, the cohesive interface elements embedded within the domain had zero thickness initially, meaning that these 4-node elements lay on the interface of the adjacent regular triangular elements. Due to the shrinkage of the sample toward the center and zero normal displacement constraint at the soil-ring interface, the nodes at this zone were displaced

409 circumferentially, leading to localized tension in some of the cohesive elements at this area.
410 Therefore, their faces were bridged by a cohesive thickness leading to a potential location for
411 crack initiation (Figure 12).
412

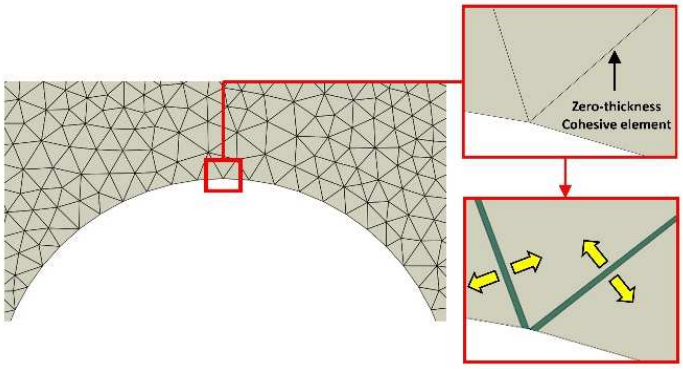

Figure 12. Embedded cohesive (interface) elements, intact and widened due to separation.

413

414 It is noted that the post-crack evaporation dynamics and deformation behavior of
415 shrinking bentonite becomes more complicated than the stage of the pre-crack desiccation
416 process where the drying of bentonite is mostly homogeneous (Lu & Dong, 2017; Peron,
417 Delenne, et al., 2009), and the constant hygroscopic expansion coefficients are thus reasonable.
418 However, the post-crack shrinkage behavior brings additional nonlinearity in the relation of
419 water decrement and volumetric shrinkage since the cracks introduce new surfaces for water to
420 evaporate. Hence, as mentioned earlier, assuming constant hygroscopic expansion coefficients
421 for the post-crack stage is a limitation in this study, while the simplification provides modeling
422 efficiency at this stage. It is required to further investigate the potential nonlinear relation due to
423 crack formation to better address the complex desiccation crack modeling.
424 To inversely identify the fracture parameters of the bentonite clay, an in-house MATLAB
425 code was developed to detect the cracks from FEM results, find the potential crack paths, and
426 carefully monitor the opening displacement of cohesive boundaries, damage extent, and water
427 content in that region of interest to be compared with DIC results. The algorithm and the process
428 of crack detection are illustrated in Figure 13.
429

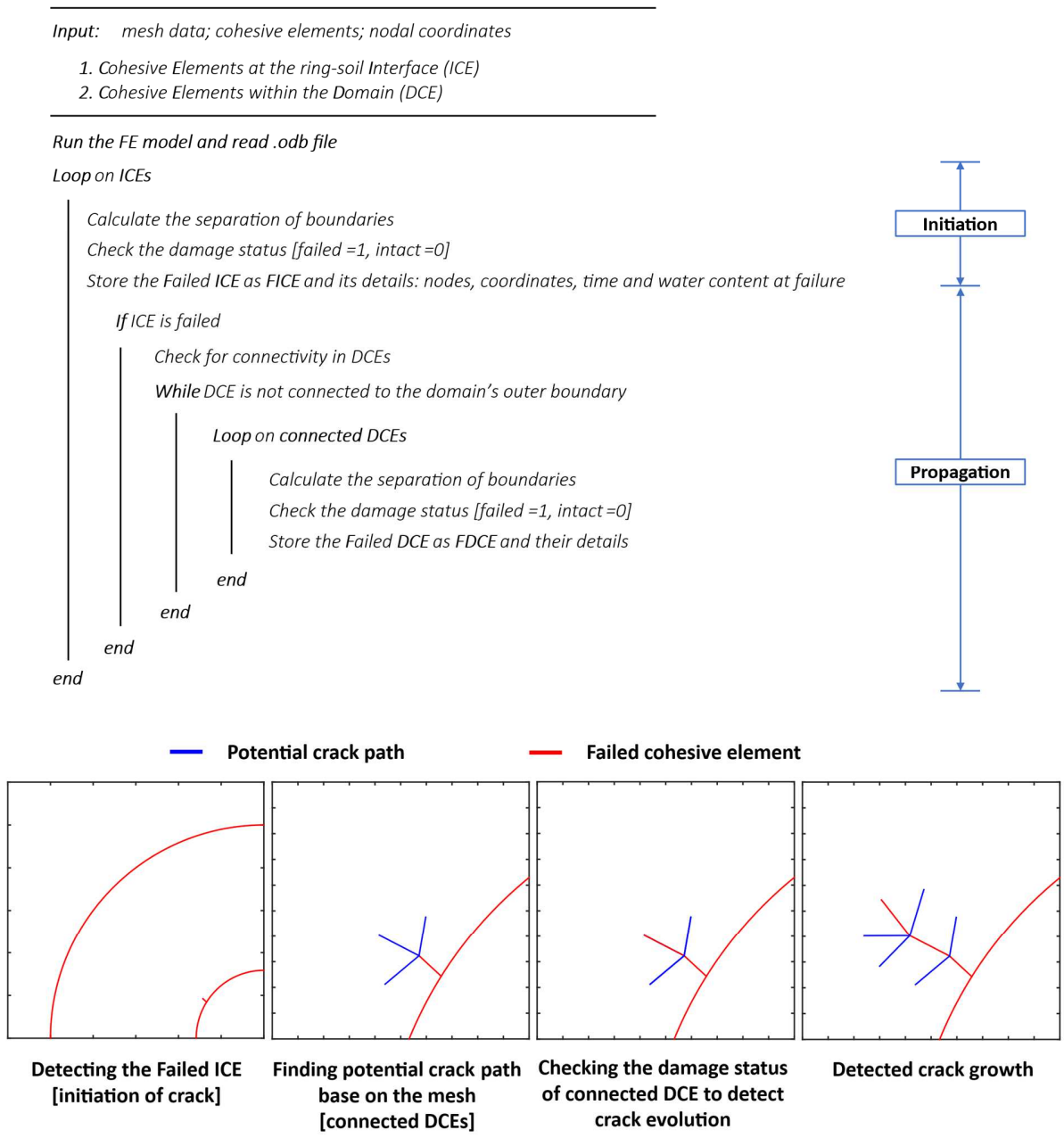

Figure 13. Crack detection: algorithm and schematic visualization.

The initiation of cracks could potentially be identified experimentally by a sudden increase in strain, which corresponds to the formation of a damaged zone. Therefore, to measure the crack initiation opening displacement of the cohesive fracture processing zone, the magnitude of the strain gradient for each node in the domain was captured and calculated using DIC data at each time step. Then, the measured relative displacement of cohesive boundaries

when a significant jump in the magnitude of strain gradient is observed was taken as the opening displacement indicating the transition of material behavior from elastic to damage-associated.

Based on the number of major cracks observed during the testing, an equivalent number of cohesive elements in which the faces were separated the most were selected as potential crack initiation locations, and the relative displacement of their boundaries was monitored at each time step of 5 minutes (0.08333 h). The bentonite sample used in the ring test usually presented two major and 1-2 minor cracks. The opening displacements of the two major cracks are exemplified in Figure 14.

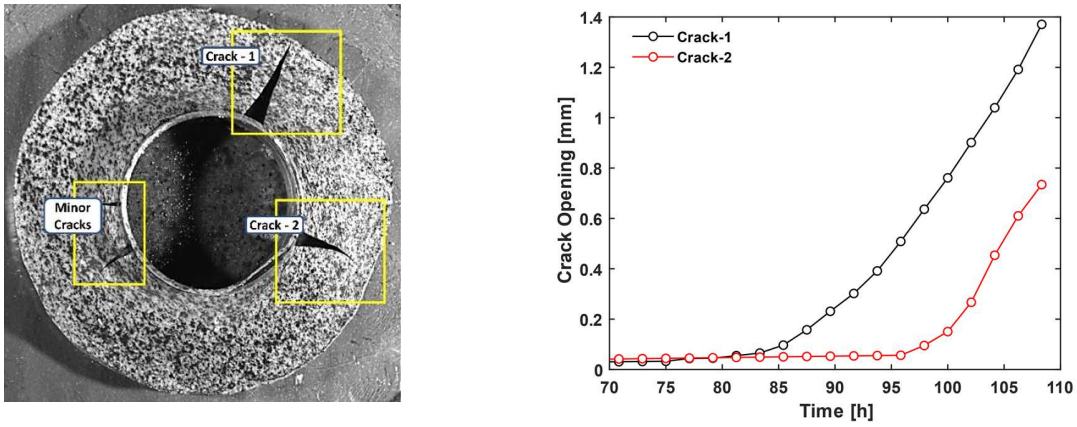

(a) (b)

Figure 14. Typical cracking pattern of desiccating bentonite: (a) crack configuration, and (b) opening displacement of two major cracks.

6.4. Cohesive zone tensile strength

In the second step of the inverse identification process, the desiccation crack initiation was studied. The mode I (i.e., opening mode) cracking was considered the major failure mechanism in this study due to the extensive tensile stress developed at the soil-ring interface. Therefore, the maximum traction at cohesive surfaces was the dominant parameter that governed the tensile cracking if it exceeded the tensile strength of the bentonite clay. The moisture-dependent cohesive zone tensile strength T_{max} (w) was defined as a power function expressed in the following equation.

$$T_{max}(w) = A.w^{-B} \quad (12)$$

where A and B are parameters that are calibrated through the DIC-FEM inverse optimization process. Parameters A and B were assumed positive values, so the tensile strength decreases with the water content increment. The crack initiation water content was another constraint set for the optimization process. Since the Young's modulus of the bentonite sample was already obtained from the experiment and the hygroscopic expansion coefficients were inversely identified in the previous step, circumferential tensile stress at the soil-ring interface can be calculated numerically. Figure 15 shows the stabilization of the normalized objective function, the optimal values of parameters A and B, and the resulting cohesive zone tensile strength as a function of gravimetric water content using the parameters identified and its comparison to other studies.

(a)

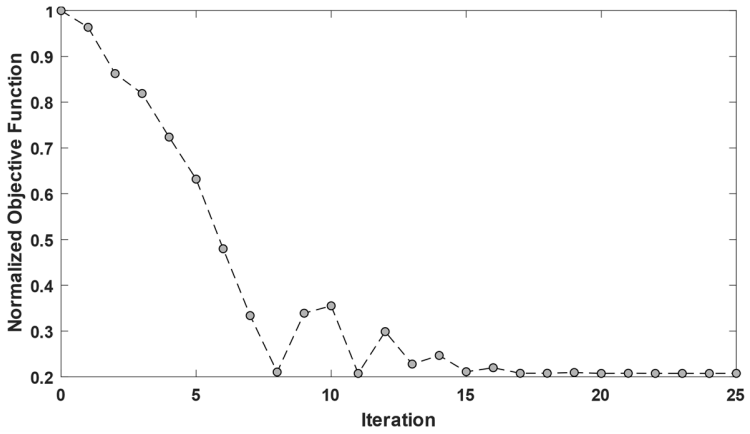

(b)

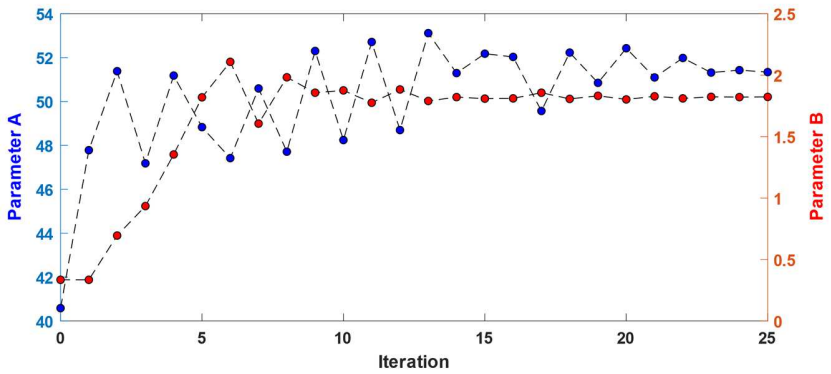

(c)

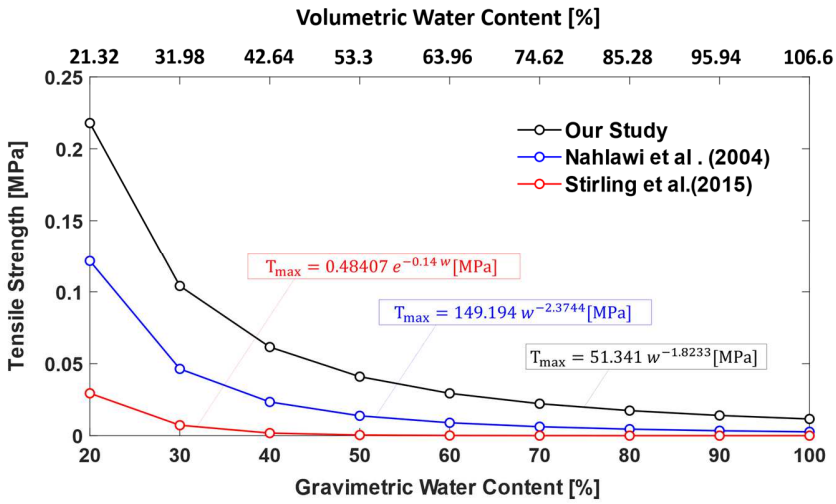

Figure 15. Inverse determination of cohesive zone tensile strength: (a) stabilized objective function value over iteration, (b) optimal model parameters saturated from the iteration, (c) cohesive zone tensile strength as a function of gravimetric water content using the material paramters identified and compared to other studies.

6.5. Cohesive zone fracture energy

The final step of inverse identification process focuses on the propagation of desiccation cracks, where the cohesive fracture energy was a primary factor. The moisture-dependent cohesive zone fracture energy was hypothesized as a power function expressed in the following form.

$$\Gamma_c(w) = C.w^{-D} \tag{13}$$

where C and D are parameters that are calibrated through the DIC-FEM inverse optimization process and w is the gravimetric water content in percent. The area under the softening part of the traction-separation curve determines the fracture energy required to fully separate the cohesive faces of an interface element. This results in the following expression.

$$C.w^{-D} = \frac{1}{2} T_{max}(w).\Delta_c \tag{14}$$

In the above equation, $T_{max}(w)$ is determined from the previous step, and Δ_c is the critical opening displacement at the complete separation of the cohesive boundaries. Initial iterations of the inverse optimization process evaluate the sensitivity of the objective function value to the unknown parameters. By considering the number of major cracks and details

(opening displacement, time and water content at crack initiation, degradation status) of cohesive elements in our FE model, and by using a MATLAB code specially-developed to detect and analyze cracks from the FEM results, the cohesive zone fracture energy was carefully characterized. The number of cracks during the desiccation process, their opening displacements, and length evolved over time were targeted to match the experiment. Figure 16 shows the progressive calibration of the two parameters over iteration and the resulting cohesive zone fracture energy as a function of gravimetric water content using the material parameters identified.

(a)

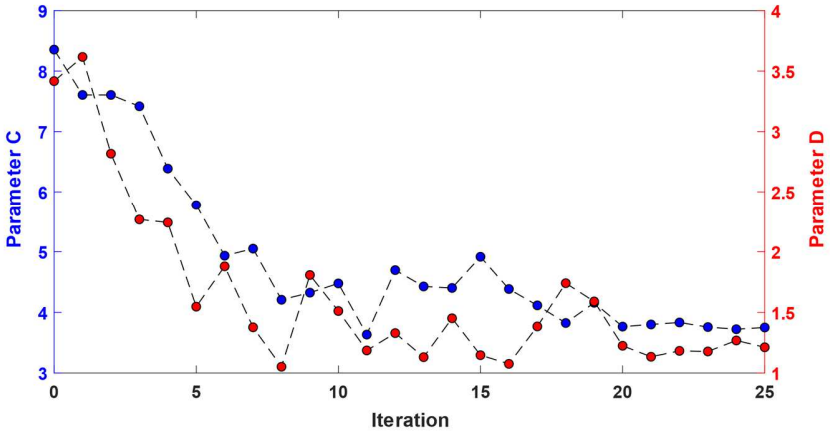

(b)

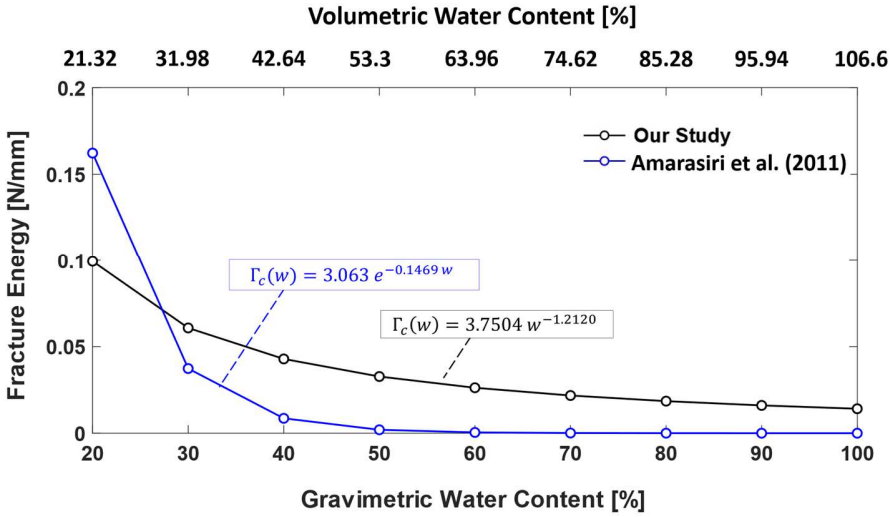

Figure 16. Inverse determination of cohesive zone fracture energy: (a) optimal model parameters saturated from the iteration, and (b) cohesive zone fracture energy as a function of gravimetric water content using the material parameters identified and compared to a study.

6.6. Further discussion

As can be seen, the fracture energy is inversely proportional to the water content. As the bentonite clay gets drier and loses more water, it becomes more brittle; hence the energy required to separate cohesive elements gradually increases. Since the maximum traction increases with moisture decrement, the critical opening displacement of cohesive boundaries should decrease. It makes sense because the bentonite with higher water content tends to deform more, and the cohesion between material boundaries endures longer. Figure 17 illustrates the evolution of traction-separation behavior with water content based on the optimal parameters obtained.

It should also be noted that the optimal parameters for the cohesive zone model and the subsequent crack pattern directly relate to the objective function criterion selected for the inverse process. With the optimal parameters for the cohesive zone model and the two hygroscopic expansion coefficients, a FE model simulation of the desiccation shrinkage followed by the cracking of a representative ring-shaped bentonite specimen was performed. Figure 18 shows the state of the desiccation process in five time-wise stages, comparing the experiment with the FE model simulation. Model simulation results agree well with the experimental observation, which implies that modeling with the material parameters obtained could effectively capture the shrinkage and desiccation cracking behavior of bentonite clay.

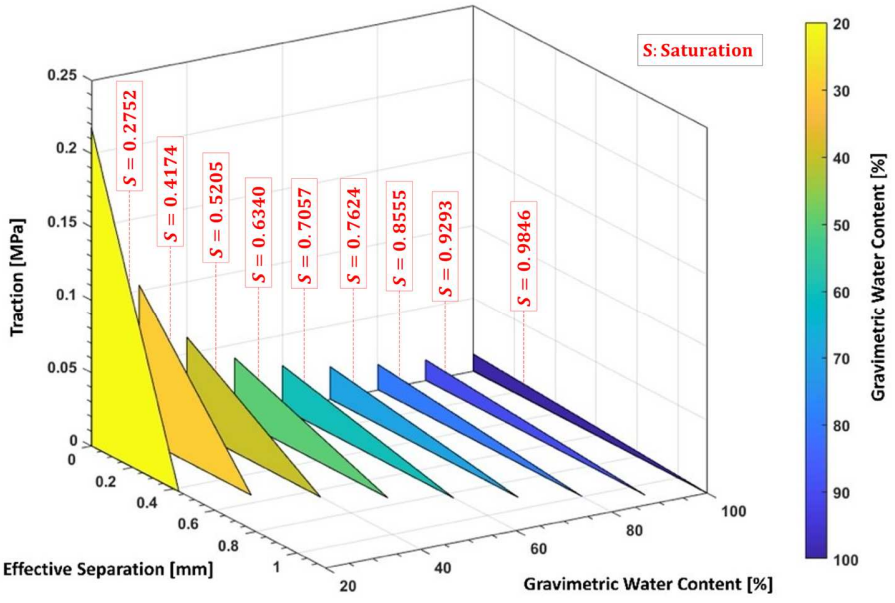

Figure 17. Evolution of the cohesive zone traction-separation behavior with moisture content based on the optimal parameters obtained.

504 The number of major cracks within the sample can vary based on multiple key factors,
505 such as sample thickness (Asahina, Houseworth, Birkholzer, Rutqvist, & Bolander, 2014). As
506 reported by Asahina et al. (2014), the sample thickness can significantly affect the number of
507 major cracks within the sample domain due to different moisture gradients, desiccation rates, and
508 consequent stress conditions. In this study, the sample was designed to be thin (1 cm thickness)
509 to minimize the effect of an in-depth moisture gradient. The reason why restrained ring testing
510 shows 2 or 3 major cracks is not certain at this stage, which requires further investigation.
511 Modeling was conducted to best simulate the experimental results by calibrating material
512 parameters. The resulting calibrated fracture parameters affect the crack initiation and
513 propagation, especially the fracture energy obtained through the inverse optimization.
514

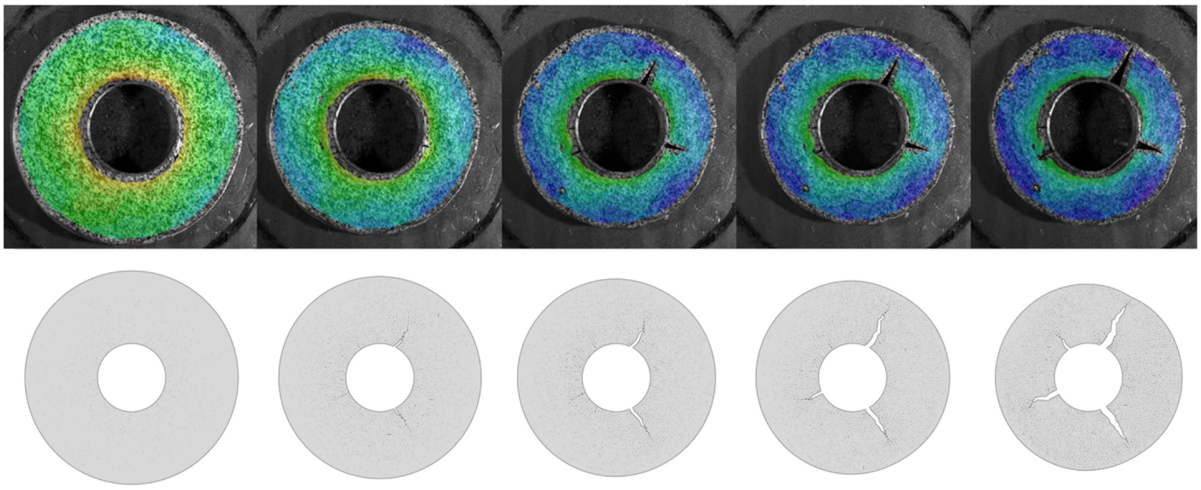

Figure 18. Comparison of desiccation process (shrinkage followed by cracking): (top) experimental results, and (bottom) FE model simulation results

515

516 In an attempt to further investigate and validate the model simulation results, the tensile
517 stress at the locations of the two primary cracks (first and second) was tracked and shown in
518 Figure 19(a). As can be seen, the first crack appeared around 10 hours earlier than the second
519 crack. The peak tensile stress for the first crack is lower than that of the second crack because the
520 clay has higher water content. The sudden drop of tensile stress implies the initiation of cracking,
521 and a partial drop for the second crack happened due to the stress release after the first crack.
522 Since the fracture energy increased with the moisture decrement, and the difference in tensile

strength at different water contents is significant, the opening displacement for the second crack should be lower to comply with the hypothesis and experimental results. The opening displacements of the two significant cracks were predicted from the FE model simulation and compared to the experimental data, as shown in Figure 19(b). The model prediction agrees well with the DIC measurements.

(a)

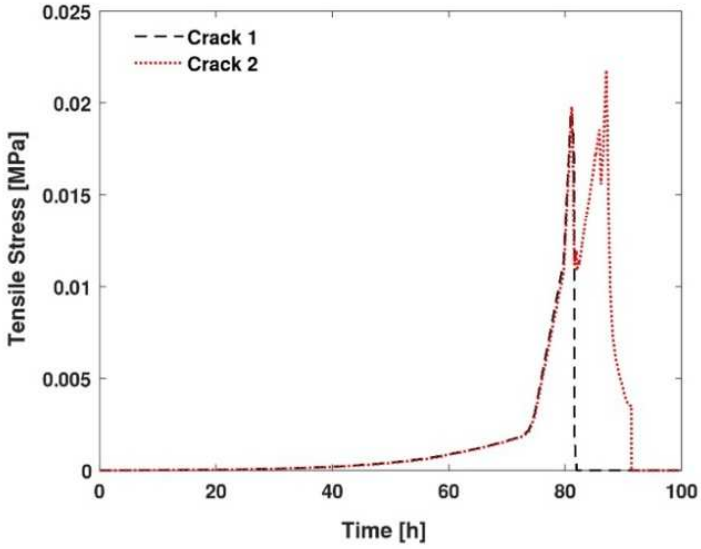

(b)

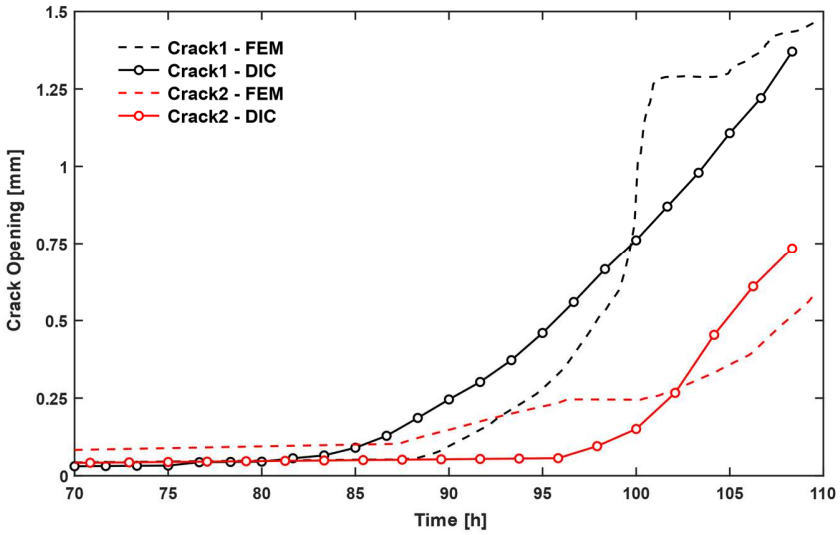

Figure 19. (a) Tensile stress at major crack locations from FEM, and (b) Numerical-Experimental validation of crack mouth opening displacement

A qualitative cross-checking with different sample replicates was carried out to ensure that the calibrated CZM parameters through the inverse optimization can justifiably represent the shrinkage-induced cracking behavior of the bentonite clay studied here. The replicates refer to samples made of the same material and tested under the same conditions, while slight variations in the initial water content and moisture loss curves were observed from these replicates, which were incorporated into their corresponding FE modeling. When the same moisture-dependent material parameters were used for the FE model with slightly different initial water content and moisture loss curves for the replicates, the resulting model simulations can differ from the previous case, as shown in Figure 20. The aim was to ensure the validity of the method and calibrated model parameters across slightly different material conditions. As shown, the FEM-DIC results are qualitatively in good agreement.

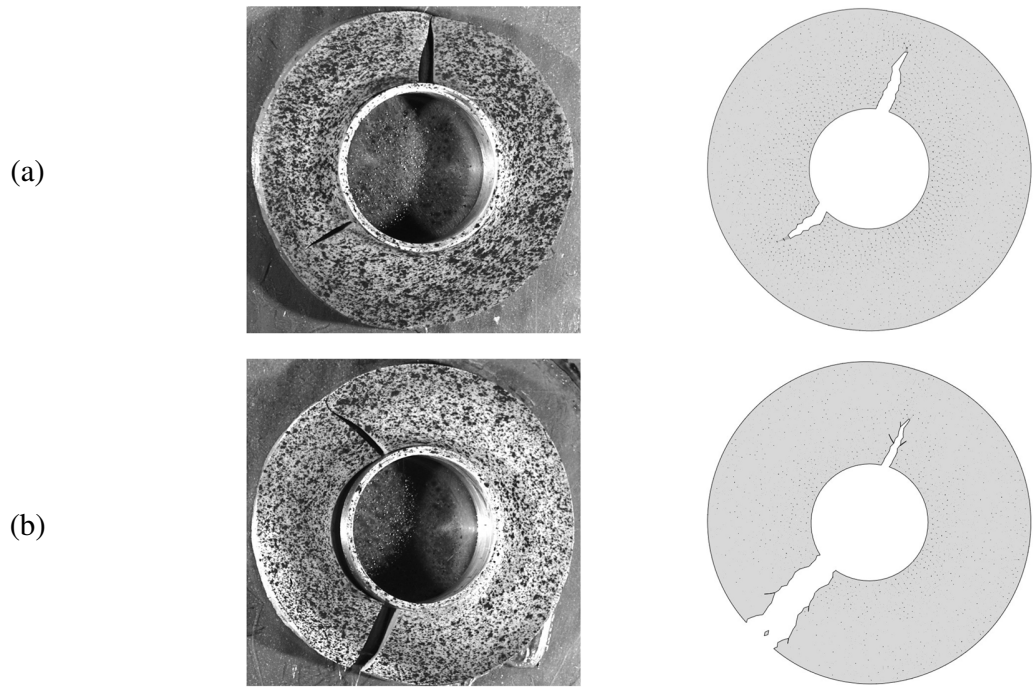

Figure 20. Final crack pattern of two other replicates: simulation (right) and test (left).

7. Summary and Conclusions

In this study, the effectiveness of using DIC-captured full-field displacement in the inverse characterization of shrinkage and fracture parameters of bentonite clay was studied. Bentonite clay is often considered in engineered barrier systems at geological repositories to

isolate the canisters filled with radioactive nuclear-spent fuels, while it is susceptible to shrink and crack due to the high temperature around the canister and the subsequent evaporation of water. This study, although limited, aimed to provide a basic understanding and characterization of the desiccation behavior of bentonite clay through integrated testing and modeling. Based on the results, the following can be concluded.

- The inverse optimization approach integrated the DIC and FEM full-field displacements to inversely identify the hygroscopic expansion coefficients and CZM fracture parameters of desiccating bentonite clay.
- A one-way coupled hydro-mechanical boundary value problem was solved by simulating the shrinkage and desiccation cracking of the bentonite clay.
- The inverse material parameter characterization was carried out in three sequentially coupled steps: in the first step, the anisotropic hygroscopic expansion coefficients were calibrated, and the simulation results of the displacement field were compared with the experiment. The second step focused on determining the cohesive zone tensile strength related to the initiation of the cracks, and the cohesive zone fracture energy was inversely identified in the final step.
- The cohesive zone model can be integrated with FEM to model random cracking due to desiccation in bentonite clay. The moisture-dependent fracture parameters can be iteratively calibrated to give a good agreement with the crack pattern between the FE model simulation results and the actual experimental (DIC) results.
- The back-calculated moisture-dependent tensile strength and fracture energy successfully modeled the initiation and propagation of desiccation cracks by complying with the time, moisture content, and opening displacements of the actual cracks captured by DIC.
- A crack detection algorithm was developed and implemented in the inverse optimization approach to address the challenge of high randomness of crack locations within the domain. This approach can be implemented in various boundary value problems.
- The experimental-computational method presented in this study can characterize material behavior subjected to complex multiphysical conditions with damage such as cracking, while further investigation to validate the approach and model in a more rigorous manner is necessary.

- It should also be noted that the modeling requires further validation with other independent experiments with different geometries and boundary conditions using the same set of material parameters identified. Furthermore, this study is limited at this stage as the testing and modeling differ from realistic conditions of materials and geologic repositories.
- The authors are currently working on integrating the approach into a more realistic multiphysical (e.g., hydro-thermal-mechanical) condition of engineered barrier systems at geological repositories. A more comprehensive set of experiments is being conducted on the effect of microfibers on shrinkage and fracture behavior of bentonite clay. Results will be presented elsewhere.

Acknowledgment

The authors appreciate the financial support from the Nuclear Energy University Programs (NEUP), Grant ID: DE-NE0008954 of Department of Energy (DOE) and the findings and conclusions do not necessarily reflect the sponsor perspectives.

References

Alonso, E. E., Alcoverro, J., Coste, F., Malinsky, L., Merrien-Soukatchoff, V., Kadiri, I., . . . Jussila, P. (2005). The FEBEX benchmark test: case definition and comparison of modelling approaches. *International Journal of Rock Mechanics and Mining Sciences, 42*(5), 611-638. doi:https://doi.org/10.1016/j.ijrmms.2005.03.004

Amarasiri, A. L., & Kodikara, J. K. (2013). Numerical modeling of desiccation cracking using the cohesive crack method. *International Journal of Geomechanics, 13*(3), 213-221.

Amarasiri, A. L., Kodikara, J. K., & Costa, S. (2011). Numerical modelling of desiccation cracking. *International Journal for Numerical and Analytical Methods in Geomechanics, 35*(1), 82-96. doi:https://doi.org/10.1002/nag.894

Asahina, D., Houseworth, J. E., Birkholzer, J. T., Rutqvist, J., & Bolander, J. E. (2014). Hydro-mechanical model for wetting/drying and fracture development in geomaterials. *Comput. Geosci., 65*, 13–23. doi:10.1016/j.cageo.2013.12.009

Byun, Y.-H., Lee, J., Cho, S., & Yoon, H. (2013). *Evaluation of void ratio and elastic modulus of unsaturated soil using elastic waves.* Paper presented at the 18th International Conference on Soil Mechanics and Geotechnical Engineering, ICSMGE 2013.

Cai, W., Gao, K., Ai, S., Wang, M., & Feng, Y. T. (2023). Implementation of extrinsic cohesive zone model (ECZM) in 2D finite-discrete element method (FDEM) using node binding scheme. *Computers and Geotechnics, 159*, 105470. doi:https://doi.org/10.1016/j.compgeo.2023.105470

Chen, H., Lv, H.-B., Chen, Z.-h., & Li, Y.-h. (2019). The Research on Strength and Deformation Behaviors of Buffer/Backfill Material under High-Temperature and High-Pressure Conditions. *Advances in Civil Engineering, 2019*, 5064690. doi:10.1155/2019/5064690

614 Chen, T., Du, M., & Yao, Q. (2022). Evolution of Hydraulic Conductivity of Unsaturated Compacted Na-
615 Bentonite under Confined Condition—Including the Microstructure Effects. *Materials,*
616 *15*(1), 219. Retrieved from https://www.mdpi.com/1996-1944/15/1/219
617 Chertkov, V. (2003). Modelling the shrinkage curve of soil clay pastes. *Geoderma, 112*(1-2), 71-95.
618 Gerbig, D., Bower, A., Savic, V., & Hector Jr, L. G. (2016). Coupling digital image correlation and finite
619 element analysis to determine constitutive parameters in necking tensile specimens.
620 *International Journal of Solids and Structures, 97*, 496-509.
621 Graupner, B. J., Shao, H., Wang, X. R., Nguyen, T. S., Li, Z., Rutqvist, J., . . . Garitte, B. (2018). Comparative
622 modelling of the coupled thermal–hydraulic-mechanical (THM) processes in a heated bentonite
623 pellet column with hydration. *Environmental Earth Sciences, 77*(3), 84. doi:10.1007/s12665-018-
624 7255-3
625 Guo, Y., Han, C., & Yu, X. (2018). Laboratory characterization and discrete element modeling of
626 shrinkage and cracking in clay layer. *Canadian Geotechnical Journal, 55*(5), 680-688.
627 Hartmann, S., Gilbert, R. R., Marghzar, A. K., Leistner, C., & Dileep, P. K. (2021). Material parameter
628 identification of unidirectional fiber-reinforced composites. *Archive of Applied Mechanics, 91*(2),
629 687-712.
630 Hassanikhah, A., Miller, G. A., & Cerato, A. B. (2021). A method to predict desiccation crack depth in a
631 compacted clayey soil. *Canadian Geotechnical Journal, 59*(4), 526-537. doi:10.1139/cgj-2020-
632 0575
633 Hobbs, P., Jones, L., Kirkham, M., Gunn, D., & Entwisle, D. (2019). Shrinkage limit test results and
634 interpretation for clay soils. *Quarterly Journal of Engineering Geology and Hydrogeology, 52*(2),
635 220-229.
636 IV, J. S., Bohnhoff, G. L., Shackelford, C. D., Benson, C. H., Sample-Lord, K. M., Malusis, M. A., & Likos, W.
637 J. (2018). Enhanced bentonites for containment of inorganic waste leachates by GCLs.
638 *Geosynthetics International, 25*(4), 392-411. doi:10.1680/jgein.18.00024
639 Junior, W., Borges, R. A., Araújo, D. L., & Pituba, J. (2021). A proposal to use the inverse problem for
640 determining parameters in a constitutive model for concrete. *Soft Computing, 25*(13), 8797-
641 8815.
642 Kim, Y.-R. (2011). Cohesive zone model to predict fracture in bituminous materials and asphaltic
643 pavements: state-of-the-art review. *International Journal of Pavement Engineering, 12*(4), 343-
644 356.
645 Kim, Y.-R., Aragao, F. T., Allen, D. H., & Little, D. N. (2010). Damage modeling of bituminous mixtures
646 considering mixture microstructure, viscoelasticity, and cohesive zone fracture. *Canadian*
647 *Journal of Civil Engineering, 37*(8), 1125-1136.
648 Kim, Y. R., Teixeira, J. E., Kommidi, S. R., Little, D. N., Aragao, F. T., Manrique-Sanchez, L., & Souza, F. V.
649 (2021). Rate-dependent fracture modeling of bituminous media using nonlinear viscoelastic
650 cohesive zone with Gaussian damage function. *Computer-Aided Civil and Infrastructure*
651 *Engineering, 36*(11), 1365-1381.
652 Kodikara, J. K., & Choi, X. (2006). A simplified analytical model for desiccation cracking of clay layers in
653 laboratory tests. *Geotechnical special publication, 147*(2), 2558.
654 Lagarias, J. C., Reeds, J. A., Wright, M. H., & Wright, P. E. (1998). Convergence Properties of the Nelder--
655 Mead Simplex Method in Low Dimensions. *SIAM Journal on Optimization, 9*(1), 112-147.
656 doi:10.1137/s1052623496303470
657 Le, T.-C., Liu, C., Tang, C.-S., Zhang, X.-Y., & Shi, B. (2022). Numerical Simulation of Desiccation Cracking
658 in Clayey Soil Using a Multifield Coupling Discrete-Element Model. *Journal of Geotechnical and*
659 *Geoenvironmental Engineering, 148*(2), 04021183.

660 Lin, Z.-Y., Wang, Y.-S., Tang, C.-S., Cheng, Q., Zeng, H., Liu, C., & Shi, B. (2021). Discrete element
661 modelling of desiccation cracking in thin clay layer under different basal boundary conditions.
662 *Computers and Geotechnics, 130*, 103931.
663 Lin, Z. Y., Tang, C. S., Yang, Z. M., Wang, Y. S., Cheng, Q., & Shi, B. (2022). Modeling of Drying-Induced
664 Soil Curling Phenomenon. *Water Resources Research, 58*(1), e2021WR029749.
665 Lu, N., & Dong, Y. (2017). Correlation between soil-shrinkage curve and water-retention characteristics.
666 *Journal of Geotechnical and Geoenvironmental Engineering, 143*(9), 04017054.
667 Lutzenkirchen, J. (2006). *Surface complexation modelling*: Elsevier.
668 Mathieu, F., Leclerc, H., Hild, F., & Roux, S. (2015). Estimation of elastoplastic parameters via weighted
669 FEMU and integrated-DIC. *Experimental Mechanics, 55*(1), 105-119.
670 McCormick, N., & Lord, J. (2010). Digital Image Correlation. *Materials Today, 13*(12), 52-54.
671 doi:https://doi.org/10.1016/S1369-7021(10)70235-2
672 Montes-H, G., & Geraud, Y. (2004). Sorption kinetic of water vapour of MX80 bentonite submitted to
673 different physical–chemical and mechanical conditions. *Colloids and Surfaces A: Physicochemical*
674 *and Engineering Aspects, 235*(1), 17-23. doi:https://doi.org/10.1016/j.colsurfa.2004.01.013
675 Nahlawi, H., Chakrabarti, S., & Kodikara, J. (2004). A Direct Tensile Strength Testing Method for
676 Unsaturated Geomaterials. *Geotechnical Testing Journal, 27*(4), 356-361. doi:10.1520/GTJ11767
677 Nelder, J. A., & Mead, R. (1965). A Simplex Method for Function Minimization. *The Computer Journal,*
678 *7*(4), 308-313. doi:10.1093/comjnl/7.4.308
679 Nsengiyumva, G., & Kim, Y. R. (2022). Field Displacement-Based Inverse Method for Elastic and
680 Viscoelastic Constitutive Properties. *Experimental Mechanics, 62*(9), 1553-1568.
681 doi:10.1007/s11340-022-00876-0
682 Ogierman, W. (2018). Inverse identification of elastic properties of constituents of discontinuously
683 reinforced composites. *Materials, 11*(11), 2332.
684 Peron, H., Delenne, J. Y., Laloui, L., & El Youssoufi, M. S. (2009). Discrete element modelling of drying
685 shrinkage and cracking of soils. *Computers and Geotechnics, 36*(1), 61-69.
686 doi:https://doi.org/10.1016/j.compgeo.2008.04.002
687 Peron, H., Hueckel, T., Laloui, L., & Hu, L. B. (2009). Fundamentals of desiccation cracking of fine-grained
688 soils: experimental characterisation and mechanisms identification. *Canadian Geotechnical*
689 *Journal, 46*(10), 1177-1201. doi:10.1139/t09-054
690 Pouya, A., Vo, T. D., Hemmati, S., & Tang, A. M. (2019). Modeling soil desiccation cracking by analytical
691 and numerical approaches. *International Journal for Numerical and Analytical Methods in*
692 *Geomechanics, 43*(3), 738-763.
693 Rahmani, M., & Kim, Y.-R. (2020). Mechanistic damage analysis of pavements: Concept and a case study.
694 In *Advances in Materials and Pavement Performance Prediction II* (pp. 224-227): CRC Press.
695 Rahmani, M., Kim, Y.-R., Park Yong, B., & Jung Jong, S. (2020). Mechanistic Analysis of Pavement Damage
696 and Performance Prediction Based on Finite Element Modeling with Viscoelasticity and Fracture
697 of Mixtures. *LHI Journal of Land, Housing, and Urban Affairs, 11*(2), 95-104.
698 doi:10.5804/LHIJ.2020.11.2.95
699 Rahmani, M., Nsengiyumva, G., Kim, Y.-R., & Hu, J. (2020). *Evaluation of Mixtures and Pavement*
700 *Performance for Rehabilitation Methods*. Retrieved from
701 Ravi, K., & Rao, S. M. (2013). Influence of Infiltration of Sodium Chloride Solutions on SWCC of
702 Compacted Bentonite–Sand Specimens. *Geotechnical and Geological Engineering, 31*, 1291-
703 1303.
704 Rutqvist, J. (2020). Thermal management associated with geologic disposal of large spent nuclear fuel
705 canisters in tunnels with thermally engineered backfill. *Tunnelling and Underground Space*
706 *Technology, 102*, 103454. doi:https://doi.org/10.1016/j.tust.2020.103454

Rutqvist, J., Börgesson, L., Chijimatsu, M., Kobayashi, A., Jing, L., Nguyen, T. S., . . . Tsang, C. F. (2001). Thermohydromechanics of partially saturated geological media: governing equations and formulation of four finite element models. *International Journal of Rock Mechanics and Mining Sciences, 38*(1), 105-127. doi:https://doi.org/10.1016/S1365-1609(00)00068-X

Rutqvist, J., Börgesson, L., Chijimatsu, M., Nguyen, T. S., Jing, L., Noorishad, J., & Tsang, C. F. (2001). Coupled thermo-hydro-mechanical analysis of a heater test in fractured rock and bentonite at Kamaishi Mine — comparison of field results to predictions of four finite element codes. *International Journal of Rock Mechanics and Mining Sciences, 38*(1), 129-142. doi:https://doi.org/10.1016/S1365-1609(00)00069-1

Rutqvist, J., Ijiri, Y., & Yamamoto, H. (2011). Implementation of the Barcelona Basic Model into TOUGH–FLAC for simulations of the geomechanical behavior of unsaturated soils. *Computers & Geosciences, 37*(6), 751-762. doi:https://doi.org/10.1016/j.cageo.2010.10.011

Rutqvist, J., Zheng, L., Chen, F., Liu, H.-H., & Birkholzer, J. (2014). Modeling of Coupled Thermo-Hydro-Mechanical Processes with Links to Geochemistry Associated with Bentonite-Backfilled Repository Tunnels in Clay Formations. *Rock Mechanics and Rock Engineering, 47*(1), 167-186. doi:10.1007/s00603-013-0375-x

Savage, D., Arthur, R., & Luukkonen, A. (2012). *Exchangeability of bentonite buffer and backfill materials*. Retrieved from Finland:

Sima, J., Jiang, M., & Zhou, C. (2014). Numerical simulation of desiccation cracking in a thin clay layer using 3D discrete element modeling. *Computers and Geotechnics, 56*, 168-180. doi:https://doi.org/10.1016/j.compgeo.2013.12.003

Singer, S., & Nelder, J. (2009). Nelder-mead algorithm. *Scholarpedia, 4*(7), 2928.

Stirling, R. A., Glendinning, S., & Davie, C. T. (2017). Modelling the deterioration of the near surface caused by drying induced cracking. *Applied clay science, 146*, 176-185. doi:https://doi.org/10.1016/j.clay.2017.06.003

Stirling, R. A., Hughes, P., Davie, C. T., & Glendinning, S. (2015). Tensile behaviour of unsaturated compacted clay soils—A direct assessment method. *Applied Clay Science, 112*, 123-133.

Systèmes, D. (2014). Abaqus analysis user's guide, version 6.14 In Dassault Systèmes. *Simulia: Rhode Island, United States.[Google Scholar]*.

Tamizdoust, M. M., & Ghasemi-Fare, O. (2022). Convective Drying Analysis of Transversely Isotropic Natural Clay. *Journal of Geotechnical and Geoenvironmental Engineering, 148*(10), 04022073. doi:doi:10.1061/(ASCE)GT.1943-5606.0002868

Tripathy, S., Tadza, M. Y. M., & Thomas, H. R. (2014). Soil-water characteristic curves of clays. *Canadian Geotechnical Journal, 51*(8), 869-883. doi:10.1139/cgj-2013-0089

Vo, T. D., Pouya, A., Hemmati, S., & Tang, A. M. (2017). Numerical modelling of desiccation cracking of clayey soil using a cohesive fracture method. *Computers and Geotechnics, 85*, 15-27.

Yan, C., Wang, T., Ke, W., & Wang, G. (2021). A 2D FDEM-based moisture diffusion–fracture coupling model for simulating soil desiccation cracking. *Acta Geotechnica, 16*(8), 2609-2628.

Yan, C., Zheng, Y., Ke, W., & Wang, G. (2021). A FDEM 3D moisture migration-fracture model for simulation of soil shrinkage and desiccation cracking. *Computers and Geotechnics, 140*, 104425. doi:https://doi.org/10.1016/j.compgeo.2021.104425

Yan, H., Jivkov, A. P., & Sedighi, M. (2023). Modelling soil desiccation cracking by peridynamics. *Géotechnique, 73*(5), 388-400. doi:10.1680/jgeot.21.00032

Yoneyama, S. (2016). Basic principle of digital image correlation for in-plane displacement and strain measurement. *Advanced Composite Materials, 25*(2), 105-123. doi:10.1080/09243046.2015.1129681

753 Zeng, L., Yu, H.-C., Gao, Q.-F., Liu, J., & Liu, Z.-H. (2022). Evolution of Tensile Properties of Compacted
754 Red Clay under Wet and Dry Cycles. *KSCE Journal of Civil Engineering, 26*(2), 606-618.
755 doi:10.1007/s12205-021-0527-6
756 Zhao, J., Jafarzadeh, S., Rahmani, M., Chen, Z., Kim, Y.-R., & Bobaru, F. (2021). A peridynamic model for
757 galvanic corrosion and fracture. *Electrochimica Acta, 391*, 138968.

758